Available online at www.sciencedirect.com
SCIENCE DIRECT
Remote Sensing of Environment 102 (2006) 99–115
Remote Sensing of Environment
www.elsevier.com/locate/rse

Land surface temperature derived from airborne hyperspectral scanner thermal infrared data

José A. Sobrino [a,*], Juan C. Jiménez-Muñoz [a], Pablo J. Zarco-Tejada [b], Guadalupe Sepulcre-Cantó [b], Eduardo de Miguel [c]

[a] Global Change Unit, Department of Thermodynamics, Faculty of Physics, University of Valencia, Valencia, Spain
[b] Instituto de Agricultura Sostenible (IAS), Consejo Superior de Investigaciones Científicas (CSIC), Córdoba, Spain
[c] Instituto Nacional de Técnica Aeroespacial (INTA), Dpto. de Observación de la Tierra, Teledetección y Atmósfera, Madrid, Spain

Received 24 October 2005; received in revised form 30 January 2006; accepted 1 February 2006

Abstract

The AHS (airborne hyperspectral scanner) instrument has 80 spectral bands covering the visible and near infrared (VNIR), short wave infrared (SWIR), mid-infrared (MIR), and thermal infrared (TIR) spectral range. The instrument is operated by Instituto Nacional de Técnica Aerospacial (INTA) and it has been involved in several field campaigns since 2004. The main goal of this paper is to analyze the feasibility of retrieving land surface temperature from the 10 AHS thermal infrared bands, from 71 to 80, located in the region between 8 and 13 μm. For this purpose, three different methods have been considered: (i) the single-channel method, which uses only one thermal band; (ii) the split-window method, which uses a combination of two thermal bands; and (iii) the TES (temperature and emissivity separation) method, which needs at least four thermal bands. The calibration of the AHS thermal bands and the algorithms have been tested with in situ measurements collected in the framework of the SPARC (Spectra Barrax Campaign) and EAGLE (Exploitation of AnGular effects in Land surfacE observations from satellites) field campaigns, which took place simultaneously in the agricultural area of Barrax (Albacete, Spain), and also in the framework of the AGRISPECTRA field campaign, carried out over an olive orchard in Córdoba (Spain), in July 2004. AHS flights were conducted at two different altitudes, 975 m and 2745 m above ground level. The results show that AHS bands 71 (8.18 μm), 72 (8.66 μm), and 73 (9.15 μm) were affected by a calibration problem. Taking into account that AHS bands 74 (9.60 μm) and 80 (12.93 μm) are located in an absorption region, bands from 75 to 79 have been finally selected for land surface temperature retrieval. The single-channel method has been applied to AHS band 75 (10.07 μm), which shows the highest atmospheric transmissivity, whereas the split-window method has been applied to the combination between bands 75 and 79 (12.35 μm), which provides the best results according to simulated data. All the AHS thermal bands ranging from 75 to 79 have been used in the TES method. The tests conducted on the different algorithms used in this study show that single-channel and split-window methods provided similar results, with root mean square errors (RMSE) between 1.6 and 1.9 K. The TES method slightly improved the results, with a RMSE of 1.4 K.

Keywords: Airborne hyperspectral scanner; Visible and near infrared; Spectral band

1. Introduction

Although remote sensing is recognized as a powerful tool in the collection, analysis, and modeling of environmental data, less attention has been given to the use of thermal infrared (TIR) remote sensing. With the launch of the NASA Terra suite of Earth remote sensing instruments in 1999, which included TIR sensors, thermal data are poised to become a major source of quantitative and qualitative information on land surface processes and for their characterization, analysis, and modelling (Quattrochi & Luvall, 2004). There are two fundamental reasons why TIR data contribute to an improved understanding of land surface processes: (i) through measurement of surface temperatures as related to specific landscape and biophysical components and (ii) through relating surface temperatures with energy fluxes for specific landscape phenomena or processes

* Corresponding author. Dr Moliner 50-46100 Burjassot, Valencia, Spain. Tel./fax: +34 96 354 31 15.
E-mail address: sobrino@uv.es (J.A. Sobrino).

0034-4257/$ - see front matter © 2006 Elsevier Inc. All rights reserved.
doi:10.1016/j.rse.2006.02.001

(Quattrochi & Luvall, 1999). Different thematic areas where TIR remote sensing data have been applied to the analysis of landscape attributes or land surface processes could be found, as for example: (i) landscape characterization, (ii) thermal intertia and landscape analysis, (iii) estimation of energy fluxes, (iv) evaporation/evapotranspiration/soil moisture, (v) quantification of energy balance or energy flux, and (vi) forest energy exchange.

In all these thematic areas and other environmental studies, land surface temperature (LST) is a key parameter which can be retrieved from TIR data. Hence, except for solar irradiance components, most of the fluxes at the surface/atmosphere interface can only be parameterized through the use of surface temperature. LST can play either a direct role, such as when estimating long wave fluxes, or indirectly as when estimating latent and sensible heat fluxes (Kerr et al., 2004). LST can be also used as an input data in water and energy balance studies, which is an important issue in environmental studies in order to achieve a better understanding on the exchange of heat and moisture between the land surface and lower atmosphere, also leading to a better understanding on the water and carbon cycles. Moreover, many other applications rely on the knowledge of LST, such as geology, hydrology, vegetation monitoring, global circulation models, and evapotranspiration, among others.

Different approaches have been published in the last years in order to retrieve LST from satellite data. However, most of these approaches have been developed for low spectral resolution sensors, with only one or two thermal bands, as the Thematic Mapper (TM) onboard the LANDSAT platform, the Advanced Very High Resolution Radiometer (AVHRR) onboard the NOAA series, the Along Track Scanning Radiometer (ATSR) onboard ERS-1 and ERS-2 platforms, and the most recent Advanced ATSR (AATSR) onboard the ENVISAT platform. Among these methods, we highlight the *single-channel* and *two-channel* or *split-window* algorithms, which will be described below. Different spectral and spatial resolution sensors are currently available, with several thermal bands as the Advanced Spaceborne Thermal Emission and Reflection Radiometer (ASTER), and the Moderate Resolution Imaging Spectrometer (MODIS) onboard Terra (or also AQUA for MODIS) satellite, or the SEVIRI (Spinning Enhanced Visible and Infrared Imager) onboard the MSG-1 (Meteosat Second Generation). Airborne sensors available are the digital airborne imaging spectrometer (DAIS), the airborne hyperspectral scanner (AHS), or the airborne reflective/emissive spectrometer (ARES), among others. Despite the methods developed for low resolution sensors that can be adapted to high resolution data, new methods have been developed in order to retrieve LST from multispectral thermal data, as the TES method (Gillespie et al., 1998).

The purpose of this paper is to analyze the feasibility of retrieving LST from AHS thermal infrared data as well as the accuracy obtained depending on the number of thermal bands used on the LST retrieval. The paper is organized as follows: in Section 2, we describe the methods used in this study for LST retrieval; in Section 3, we present the field campaigns and ground-based measurements; and in Section 4, we describe the AHS sensor. The results obtained are shown in Section 5, which includes the analysis of the calibration of the AHS thermal bands and the tests and validation conducted on the algorithms. Finally, we present the conclusions drawn in this study.

2. Methods for LST retrieval

Different methods or techniques have been proposed in the last years in order to retrieved LST from thermal infrared data. A review of methods can be found in Sobrino et al. (2002), Dash et al. (2002), and Kerr et al. (2004). Basically, these methods could be classified as (i) single-channel methods, which used only one thermal band; (ii) two-channel or split-window methods, which use a combination between two thermal bands; and (iii) two-angle methods, which use one thermal band and two view angles. There are also other methods, which use more than two thermal bands or based on other techniques (see for example Becker & Li, 1990a; Sun & Pinker, 2003; Wan & Li, 1997). The availability of sensors with multispectral capabilities in the thermal infrared region has also favoured the development of methods for LST retrievals, which use several thermal bands, as the temperature and emissivity separation (TES) method, developed by Gillespie et al. (1998), which also provides surface emissivities jointly with the temperature. In order to retrieve LST from AHS data, we considered the single-channel, two-channel, and TES methods, which are widely used by the scientific community and described below.

2.1. Theoretical background

Methods for LST retrieval based on the radiative transfer equation, which can be written in the thermal infrared region for a certain sensor band i as:

$$L_i(T_i) = L_i^{\mathrm{LLR}}\tau_i + L_i^{\uparrow} \tag{1}$$

where $L_i(T_i)$ is the radiance measured by the sensor (T_i is the at-sensor brightness temperature), τ_i is the atmospheric transmissivity, and $L_i^{\uparrow}$ is the up-welling path radiance. The term L^{LLR} is the land-leaving radiance (LLR) or radiance measured at ground-level, which is given by:

$$L_i^{\mathrm{LLR}} = \varepsilon_i B_i(T_s) + (1-\varepsilon_i)\frac{F_i^{\downarrow}}{\pi} \tag{2}$$

where ε_i is the surface emissivity, $B_i(T_s)$ is the Planck radiance at surface temperature T_s, and $F_i^{\downarrow}$ is the down-welling sky irradiance. In Eq. (2), the assumption of Lambertian behaviour for the surface has been considered in order to express the reflection term as $(1-\varepsilon)\pi^{-1}F^{\downarrow}$. The magnitudes involved in Eqs. (1) and (2) are band averaged values using the spectral response functions.

2.2. Single-channel method

Single-channel methods retrieve LST only from one thermal band. Different single-channel algorithms can be found in the

literature (see for example Jiménez-Muñoz & Sobrino, 2003; Qin et al., 2001). In this paper, we propose a single-channel algorithm based on the solving for the Planck radiance according to Eqs. (1) and (2):

$$B_i(T_s) = \frac{L_i(T_i) - L_i^{\uparrow}}{\varepsilon_i \tau_i} - \frac{(1-\varepsilon_i)F_i^{\downarrow}/\pi}{\varepsilon_i} \quad (3)$$

LST can be finally retrieved by inversion of the Planck's law:

$$T_s = \frac{c_2}{\lambda_i}\left[\ln\left(\frac{c_1}{\lambda_i^5 B_i}+1\right)\right]^{-1} \quad (4)$$

where B_i is given by Eq. (3), and c_1 and c_2 are the constants in the Planck's function ($c_1 = 1.19104\times10^8$ W μm^4 m^{-2} sr^{-1} and $c_2 = 14387.7$ μm K). In this method, the surface emissivity ε_i is assumed to be known. Assuming that atmospheric water vapour is the primary factor controlling the magnitude of atmospheric transmittance, the hemispheric down-welling radiance and up-welling atmospheric radiance for a given band, different approaches can be proposed in order to related these atmospheric parameters with the atmospheric water vapour, which is a more easily accessible parameter. The results obtained will be shown in Section 3. This procedure has been applied to high resolution data by Jiménez-Muñoz and Sobrino (2005), providing good results (root mean square errors RMSE < 1.8 K) for atmospheres with low water vapour content and using the thermal band for which the atmospheric transmissivity is higher.

2.3. Two-channel algorithms

The basis of the two-channel technique (or split-window when it is applied in the region 10–12.5 μm) is that the atmospheric attenuation suffered by the surface emitted radiance is proportional to the difference between the at-sensor radiances measured simultaneously in two different thermal channels (McMillin, 1975). Many papers have used this technique to extract sea surface temperature (Deschamps & Phulpin, 1980; McClain et al., 1985; Sobrino et al., 1993a, etc.) and land surface temperature (Becker & Li, 1990b; Prata, 1993; Price, 1984; Sobrino et al., 1991, 1994, etc.). In this paper, the two-channel algorithm proposed by Sobrino and Raissouni (2000) has been used, which takes into account the emissivity and water vapour effects:

$$T_s = T_i + a_1(T_i - T_j) + a_2(T_i - T_j)^2 + a_0 + (a_3 + a_4 w)(1-\varepsilon) + (a_5 + a_6 w)\Delta\varepsilon \quad (5)$$

where T_s is the surface temperature (in K), T_i and T_j are the at-sensor brightness temperatures of the different thermal DAIS channels (in K), $\varepsilon = (\varepsilon_i + \varepsilon_j)/2$ and $\Delta\varepsilon = (\varepsilon_i - \varepsilon_j)$ are the mean effective emissivity and the emissivity difference, w is the total atmospheric water vapour (in g/cm^2), and, finally, a_k ($k = 0$ to 6) are the numerical coefficients of the two-channel algorithm. These coefficients can be obtained by means of a simulation procedure, which will be described in Section 3.

2.4. TES method

The TES (temperature and emissivity separation) method estimates land surface emissivity ε_i and temperature T_s from multispectral thermal data. The TES algorithm is described in detail in Gillespie et al. (1998), so a detailed description of the method will not be given here. It is based on the radiative transfer equation (see Eqs. (1) and (2)) applied to each thermal band and it is composed by three modules (NEM, RATIO, and MMD). The method uses atmospherically corrected data (land-leaving radiance and down-welling atmospheric irradiances) and a semi-empirical relation determined from laboratory spectra, between the minimum emissivity (ε_{min}) and spectral contrast (maximum–minimum difference, MMD). The semi-empirical relation between ε_{min} and MMD has been originally calculated for the ASTER sensor onboard the Terra platform, with five thermal bands in the region between 8 and 12 μm. Using 86 laboratory spectra, Gillespie et al. (1998) found the following simple power law:

$$\varepsilon_{min} = 0.994 - 0.687\,\mathrm{MMD}^{0.737} \quad (6)$$

with a correlation coefficient squared of $R^2 = 0.983$ and 95% of the samples falling within ±0.02 emissivity units. Once the surface emissivities have been recovered, LST is obtained by inversion of the Planck's law according to Eq. (4) and using the thermal band for which the emissivity is maximum, in order to minimize the effect of the sky irradiance in the reflection term.

3. Field data

Field campaigns are of importance in order to validate or test the algorithms developed for retrieving a certain bio-geophysical parameter from satellite or aircraft data. The aircraft images and the in situ data used in order to conduct the study shown in this paper were acquired in the framework of three field campaigns related to three different projects. The SPARC (Spectra Barrax Campaign, http://gpds.uv.se/sparc) and EAGLE (Exploitation of AnGular effects in Land surfacE observations from satellites, http://www.uv.es/ucg/eagle) field campaigns took place simultaneously in the Barrax test site (Albacete, Spain), in 2004. Another field campaign was conducted in 2004 in an olive orchard located in Córdoba (Spain), in the framework of the AGRISPECTRA (Estimation of Leaf and Crop Biophysical Variables in Olive and Vineyard Canopies through Hyperspectral Remote Sensing Methods for Integration with Precision Agriculture) project. The Barrax test site is an agricultural area situated in the West of the province of Albacete, 28 km from the capital town (39°3′N, 2°6′W) (Moreno et al., 2001). Fig. 1 shows the study area of Barrax from an AHS image acquired on 15 July 2004 at 12:43 UTC, in which the plots where field measurements were carried out are also displayed. The Córdoba site is a 4 ha irrigated olive orchard (*Olea europaea* L. cv. 'Arbequino') located in southern Spain (37.8°N, 4.8°W). A full description of this experimental area be found in Sepulcre-Cantó et al. (in press). Fig. 2 shows the study area from an AHS image acquired on

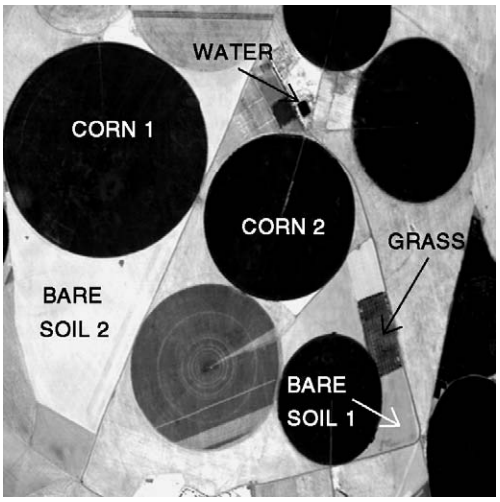

Fig. 1. The study area of Barrax. The image corresponds to AHS band 75 (10.07 μm) raw data and it was acquired on 15 July 2004 at 12:43 UTC, with a pixel size of 7 m.

25 July 2004 at 9:30 UTC, in which the olive orchard is highlighted.

In the SPARC/EAGLE field campaign, temperature measurements were made using different broadband and multiband field thermal radiometers. Models EVEREST 3000, RAYTEK ST8, and RAYTEK MID correspond to broadband radiometers, whereas models CIMEL CE 312-1 and CIMEL CE 312-2 ASTER are multiband radiometers (they also have a broad band). In addition, two blackbodies (EVEREST 1000 and GALAI 204-P) were used for calibration purposes. Table 1 summarizes the main technical characteristics of the thermal radiometers. Field measurements were made over two plots of bare soil (referred as 'bare soil 1' and 'bare soil 2') and two plots of corn (referred as 'corn 1' and 'corn 2'), one plot of water and one plot of grass (see Fig. 1). Two different techniques were considered in order to measure surface temperatures: (i) by means of transects, i.e., measuring while walking along the field, and (ii) by means of fixed measurements by placing the radiometers on poles with an altitude of around 2 m.

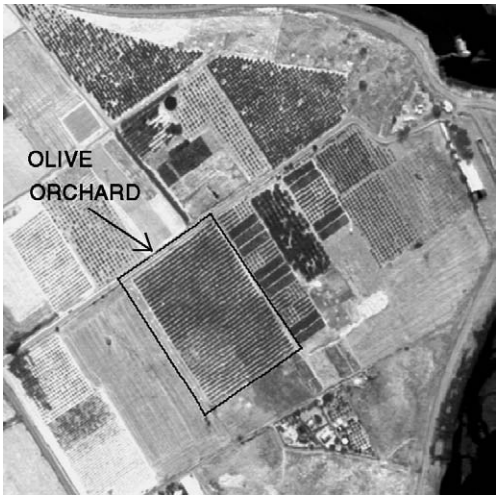

Fig. 2. The study area of Córdoba. The image has been obtained from the at-sensor radiance in AHS band 75 (10.07 μm) and it was acquired on 25 July 2004 at 9:30 UTC, with a pixel size of 2.5 m.

Table 1
Main technical specifications for the field radiometers (FOV: field of view)

Model	Bands μm	Range °C	Accuracy °C	FOV °C
CIMEL 312-1	8–13	−80 to 60	0.1	10
	8.2–9.2			
	10.3–11.3			
	11.5–12.5			
CIMEL 312-2	8–13	−80 to 60	0.1	10
	11–11.7			
	10.3–11			
	8.9–9.3			
	8.5–8.9			
	8.1–8.5			
EVEREST 3000	8–14	−40 to 100	0.5	4
RAYTEK ST8	8–14	−30 to 100	0.5	8
RAYTEK MID	8–14	−40 to 600	0.5	20

A total of 10 infrared sensors Apogee model IRTS-P were placed on poles with an altitude of 6 m over 10 olive trees in the Cordoba site (AGRISPECTRA project) in order to monitor crown temperature continuously as function of a tree water status gradient obtained through drip irrigation method. Previous to the field installation, the IRT sensors were calibrated in the laboratory and under natural sun conditions to study the IRT response to the diurnal temperature variation. Temperature over the course of the day varied between 25 °C and 40 °C, enabling a comparison between the IRT-estimated temperature and a thermocouple type K (chromel–alumel) in contact with the water target used for calibration. The observed errors agreed with the sensitivity of the instrument (Apogee, www.apogee-inst.com) yielding a deviation of ±0.4 °C between the 5 °C and 40 °C range. The 52° field-of-view (FOV) of the IRTS-P sensors placed on the top of each olive tree at 1 m distance from the crown enabled the measurement of an integrated canopy temperature for each single tree crown.

4. The AHS sensor

4.1. Technical characteristics

The airborne hyperspectral scanner (AHS) (developed by SensyTech Inc., currently ArgonST, USA) is operated by the Spanish Institute of Aeronaoutics (INTA) and it was placed onboard the aircraft CASA 212-200 *Paternina*. The AHS sensor is based on the integration of many advanced technologies developed by SenSyTech under R&D contracts over the past few years. While the combination of these components is offered here for the first time, each of the individual items has been delivered and field-tested in operational use. The AHS incorporates advanced components to ensure high performance while maintaining the ruggedness to provide operational reliability in a survey aircraft. The main AHS technical specifications and the arrangement of the spectral bands are 80 bands in four ports (VIS, NIR, SWIR, MWIR, and LWIR);

Table 2
AHS thermal bands

Band	FWHM (μm)	Effective wavelength (μm)
71	7.95–8.42	8.18
72	8.45–8.84	8.66
73	8.94–9.35	9.15
74	9.38–9.81	9.60
75	9.85–10.27	10.07
76	10.31–10.86	10.59
77	10.89–11.45	11.18
78	11.49–12.05	11.78
79	12.09–12.57	12.35
80	12.65–13.14	12.93

FOV: 90° (±45°), IFOV: 2.5 mrad, GFOV: 2–6 m at 140 kt cruise speed; scan speed: 6.25, 12.5, 18.75, 25, 31.25, 35 rps; 12 bits digitised; 750 samples per line; black body thermal references (set to 15 °C and 55 °C). The arrangement of the AHS thermal bands from 71 to 80 is given in Table 2.

4.2. Imagery acquired

During the SPARC/EAGLE campaign, the AHS flights took place in 2 days, 15 July 2004 (flight 1) and 18 July 2004 (flight 2). Flight 1 started at 10:43 UTC and finished at 12:45 UTC. It was composed by 7 AHS images acquired at low altitude (975 m above ground level—AGL, pixel size 2.5 m) and 2 AHS images acquired at high altitude (2745 m AGL, pixel size 7 m). Flight 2 started at 10:30 UTC and finished at 12:20 UTC, also composed by seven images at low altitude and two images at high altitude (same characteristics as flight 1, but different line flights).

In the AGRISPECTRA campaign, three AHS images were carried out on 25 July 2004 at different times: 7:30 GMT (flight 1), 9:30 GMT (flight 2), and 12:30 GMT (flight 3). The flights had similar characteristics to the low flights conducted in SPARC/EAGLE, with an altitude of 980 m AGL and a pixel size of 2.5 m.

4.3. AHS data processing and atmospheric correction

The processing of the AHS imagery included the raw data to radiance transformation and the atmospheric correction. AHS images were processed to at-sensor radiance for the thermal infrared bands (from 71 to 80) using calibration coefficients determined during flight from two blackbody sources which are viewed for every mirror scan. The first (cool) blackbody has been set to 15 °C, whereas the second (warm) blackbody had been set to 55 °C. This procedure is performed for every thermal band on every scanline. The AHS onboard blackbodies are copper plates covered with a black paint with emissivity greater than 0.99 through the 3 to 14 μm spectral range (note that this specification permits a bias <0.5 °C in the measured temperature), and they subtend 4° when viewed by the radiometer. The performance of the thermal control is not specified by the manufacturer and we have observed some temporal instabilities. So, we use the actual line-by-line blackbody data in the calibration instead of the nominal or average one. As the temporal variations show a low frequency, we have not considered the possible delay in the response of the measuring thermistors as a source of error. Circuitry to monitor the blackbodies temperature (YSI Thermilinear thermistors network) is designed to yield better than 0.5° accuracy (including the sensors). The non-linearity effects are limited to ±0.15 °C.

The atmospheric correction of AHS images was performed using the radiative transfer equation given by Eq. (1), from which the land-leaving radiance (L_i^{LLR}) can be obtained from the at-sensor radiance after compensation of atmospheric effects according to:

$$L_i^{\mathrm{LLR}} = \frac{L_i(T_i) - L_i^{\uparrow}}{\tau_i}. \tag{7}$$

The atmospheric parameters τ_i, $F_i^{\downarrow}$, and $L_i^{\uparrow}$ involved in the atmospheric correction were estimated using the MODTRAN 4 radiative transfer code (Berk et al., 1999) and the in situ

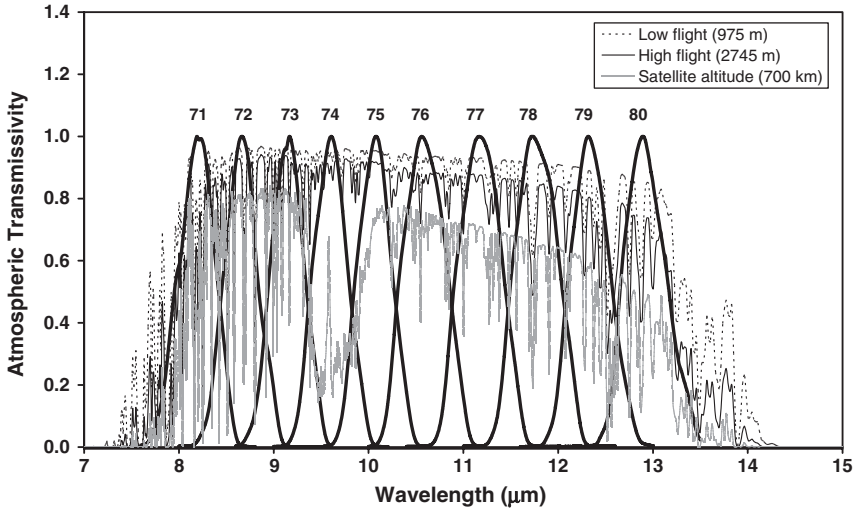

Fig. 3. Location of the AHS thermal bands. The plot also shows the atmospheric transmissivity spectrum overlayed with the location of the AHS thermal bands for the low (975 m AGL) and high (2745 m AGL) flights carried out on 15 July 2004 and also for a typical satellite altitude (700 km).

radiosoundings launched almost simultaneously with the AHS overpass. The band values were finally obtained using the filter functions of the AHS thermal bands. These filter functions are shown in Fig. 3 compared to the atmospheric transmissivity for the low flight (975 m AGL), the high flight (2745 m AGL), and a typical satellite altitude (700 km). Bands 71 and 80, located around 8 and 13 μm, respectively, show the highest atmospheric absorption, whereas bands 75 to 79 are located in the atmospheric window 10–12.5 μm, with band 75 showing the highest atmospheric transmissivity. Band 74 is located in the region of the ozone absorption, but in the AHS flights this absorption is not observed because the maximum absorption of the ozone is usually located at atmospheric altitudes higher than 10 km.

5. Results and analysis

5.1. LST estimation from ground-based measurements

The thermal radiometers described in Section 3 and used at ground-level measure the land-leaving radiance (L^{LLR}) given by Eq. (2), since at ground-level is assumed that $\tau \approx 1$ and $L^{\uparrow} \approx 0$. Surface emissivity values (ε) can be measured in situ, for example using the box method (Nerry et al., 1990), or extracted from spectral libraries, as for example the ASTER spectral library (http://speclib.jpl.nasa.gov), whereas $F^{\downarrow}/\pi$ can be approximately measured by pointing with the radiometer to the sky with a near-nadir view or, more accurately, by pointing to the sky with a view angle of 53° measured from the zenith (Kondratyev, 1969). Therefore, from Eq. (2), it is possible to find the value of T_s from ground-based measurements and by inversion of the Planck's law. The term 'radiometric temperature' (T_{rad}) is used when Planck's law is inverted using the quantity L^{LLR}, so the difference between the land surface temperature (T_s) and the radiometric temperature (T_{rad}) is due to the emissivity (ε) and atmospheric effects ($F^{\downarrow}$), both coupled.

In order to illustrate the differences between radiometric and land surface temperatures and also the problems related with the thermal heterogeneity of the natural surfaces, Fig. 4 shows an example of the T_s and T_{rad} values obtained with the Raytek MID radiometer fixed on the mast between 13:00 and 13:15 LT (local time, GMT = LT − 2) the 15th of July in 2004 over bare soil (Fig.

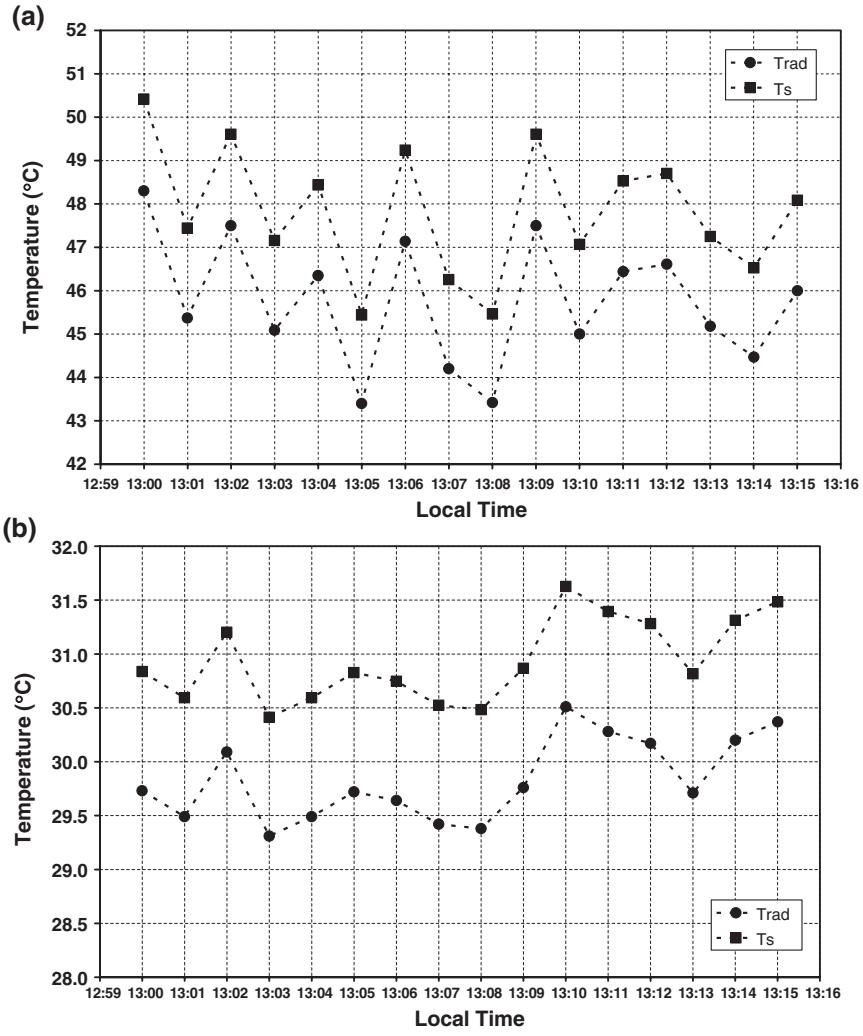

Fig. 4. Radiometric temperature (T_{rad}) and surface temperature (T_s) measured with the Raytek MID radiometer located on fixed masts over (a) bare soil and (b) green grass.

4a) and grass (Fig. 4b) in the Barrax site. The difference between T_s and T_{rad} is higher for bare soil (around 2 K) than for green grass (around 1 K), due to the higher emissivity for green grass. Surfaces with high surface emissivity minimize the effect of the emissivity and atmospheric correction. The graphs included in Fig. 4 also show a higher heterogeneity for bare soil than for green grass. Hence, the difference between the maximum and minimum value for bare soil is 5 K, whereas for green grass is 1.2 K. Moreover, differences between two consecutive measurements (in steps of 1 min) are higher than 1.5 K for bare soil but lower than 0.5 K for green grass. The heterogeneity of the surfaces can be also shown by calculating the mean value and the standard deviation of the measurements. Values of T_s = (321.0 ± 1.5) K for bare soil and T_s = (304.1 ± 0.4) K for green grass have been obtained, showing a higher standard deviation for bare soil. Another example is presented in Fig. 5, which shows a comparison between the values measured with the Raytek MID radiometer located on fixed masts and the values measured with the Raytek ST8 radiometer by making transects around the same sample for bare soil and green grass. This figure shows a significant variability in the measurements carried out by transects, as has been stated before. The differences between the fixed measurements and the transect measurements are also lower for green grass, which is a more homogeneous surface. The variability shown in the radiometric temperatures can be also due to turbulence induced fluctuations of wind speed at the surface (Balick et al., 2003). These fluctuations can be larger than 1 K, so accuracies worse than 1 K are always expected in the validation procedures. These examples illustrate the difficulties involved in the field measurements and the validation of satellite products, mainly over heterogeneous surfaces.

5.2. Analysis of the AHS thermal data: calibration and optimal bands

Eqs. (1) and (2) can be used in order to reproduce the radiance measured by the sensor (L_i) or the at-sensor brightness temperature (T_i) (by inversion of the Planck's law) if the atmospheric parameters (τ_i, $F_i^{\downarrow}$, and $L_i^{\uparrow}$), the emissivity spectrum

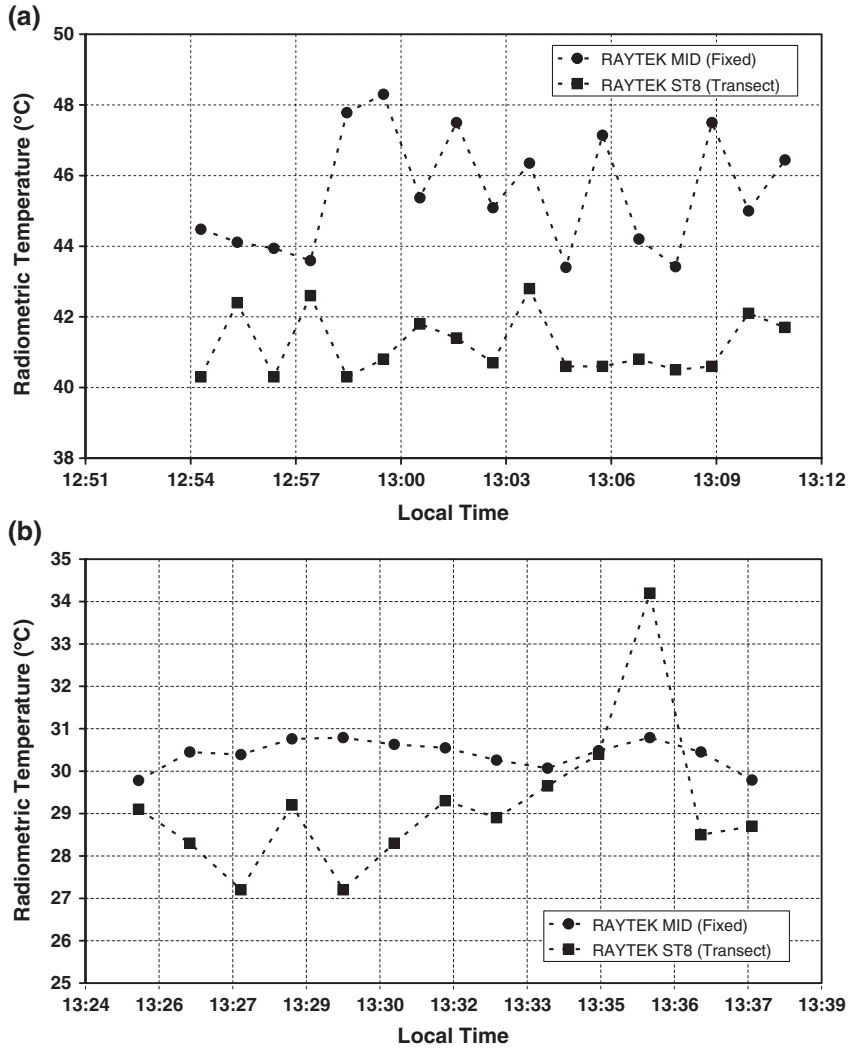

Fig. 5. Comparison between the radiometric temperature measured with the Raytek MID radiometer located on fixed masts and the radiometric temperature measured with the Raytek ST8 radiometer by making transects over (a) bare soil and (b) green grass.

(ε_i), and the LST (T_s) are known. Values of at-sensor brightness temperatures have been compared with the extracted from the AHS images (by selecting boxes of $m \times n$ pixels located around the measurement sites) in order to check the calibration of the AHS sensor. The atmospheric parameters have been extracted from the radiosoundings launched in situ and the MODTRAN 4 code. The emissivity spectra for water and grass have been obtained from the ASTER spectral library, whereas for the corn plot a constant value of 0.99 have been assumed due to its high coverage. One sample of soil was collected at the field and sent to the Jet Propulsion Laboratory (JPL) in order to measure its emissivity spectrum. Fig. 6 shows all the emissivity spectra for the AHS thermal bands considered in this study. The analysis is only shown for the SPARC/EAGLE campaign, since in the AGRISPECTRA campaign the atmosphere was not characterized. From all the AHS images and ground-based measurements available, only the plots measured simultaneously with the sensor overpass have been selected for checking the calibration of the AHS thermal bands, leading to a total amount of 19 plots acquired over different surfaces (bare soil, grass, corn, and water). The results obtained are shown in Fig. 7 for the high flight (975 m AGL) and in Fig. 8 for the low flight. All the graphs shown in these figures have been scaled in steps of 1 K (*Y*-axis, horizontal lines) for a better comparison of the differences obtained over the different plots and flights. According to the results obtained, AHS band 73 (9.15 μm) seems to be affected by a calibration problem, because the values obtained with this band do not follow the expected tendency in the shape of the brightness temperatures versus the wavelength. AHS band 71 (8.183 μm) also shows some calibration problems in the low flights (see Fig. 8), whereas band 72 (8.659 μm) seems to show a random behaviour. Looking to the different plots considered in this analysis, the results obtained over water provide, in general, the better accordance with the ground-based measurements. It should be noted that the water behaviour is similar to a blackbody, so the emissivity and reflection terms $(1-\varepsilon)\pi^{-1}F^{\downarrow}$ involved in Eq. (2) have a minimal contribution. The bare soil plot provides a good shape for the spectrum; however, high differences (>4 K) have been found, except for the bare soil observed in the AHS image acquired on 18 July at 11:03 UTC (low flight, Fig. 8). An explanation of the different behaviour of this bare soil and the others could be found in the different radiometers used in the measurements. This last bare soil plot was measured with the CIMEL radiometer, which is the most accurate thermal radiometer. Problems on the ground-based measurements have been also found in the corn plots for the low flight carried out on 18 July at 11:03 UTC (see Fig. 8). Differences when comparing with ground-based measurements higher than 4 K have been obtained. The corn plot for the AHS image acquired at 10:50 UTC (also included in Fig. 8) shows ground-based brightness temperatures substantially different to those measured at 11:03 UTC. Taking into account that the corn plot was in a fully covered stage and well irrigated, temperatures between the two consecutive flights should be similar. Significant differences have been found also in some green grass plots. Despite these plots have been labelled as "green", a visual inspection at the field site shows a mixed contribution composed by green and also senescent grass, leading to a less homogeneous plot. Despite these problems, the AHS thermal bands provides good results in comparison with ground-based measurements for the bands located in the split-window region from 10 to 13 μm (AHS bands from 75 to 79).

5.3. Simulated data for single-channel and split-window algorithms

In order to obtain operative algorithms for retrieving LST with single-channel or split-window methods, different atmospheric conditions have been simulated. For this purpose the MODTRAN 4 radiative transfer code (executed in the thermal radiance mode) and a set of 54 radiosoundings extracted from

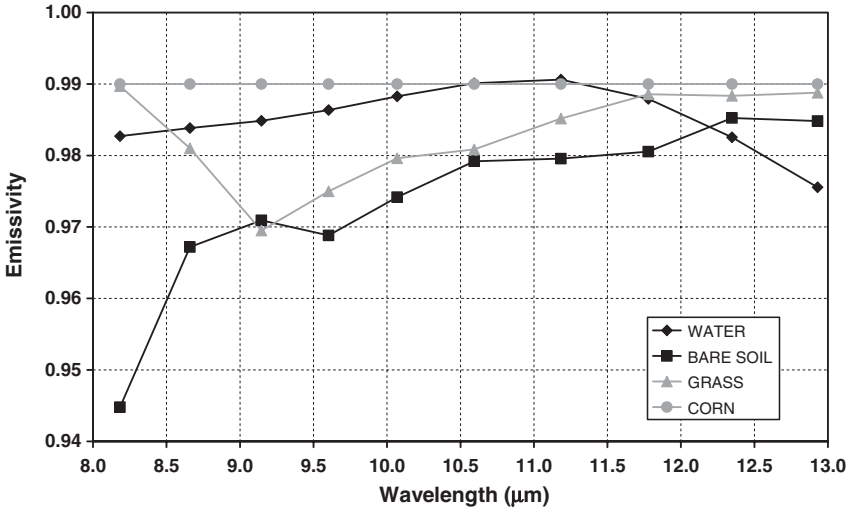

Fig. 6. Emissivity spectra for different plots. Emissivities for water and grass have been extracted from the ASTER spectral library, whereas the bare soil sample was collected at the field and measured in the Jet Propulsion Laboratory (JPL). A constant value equal to 0.99 has been considered for the corn plot, due to its greenness and high cover.

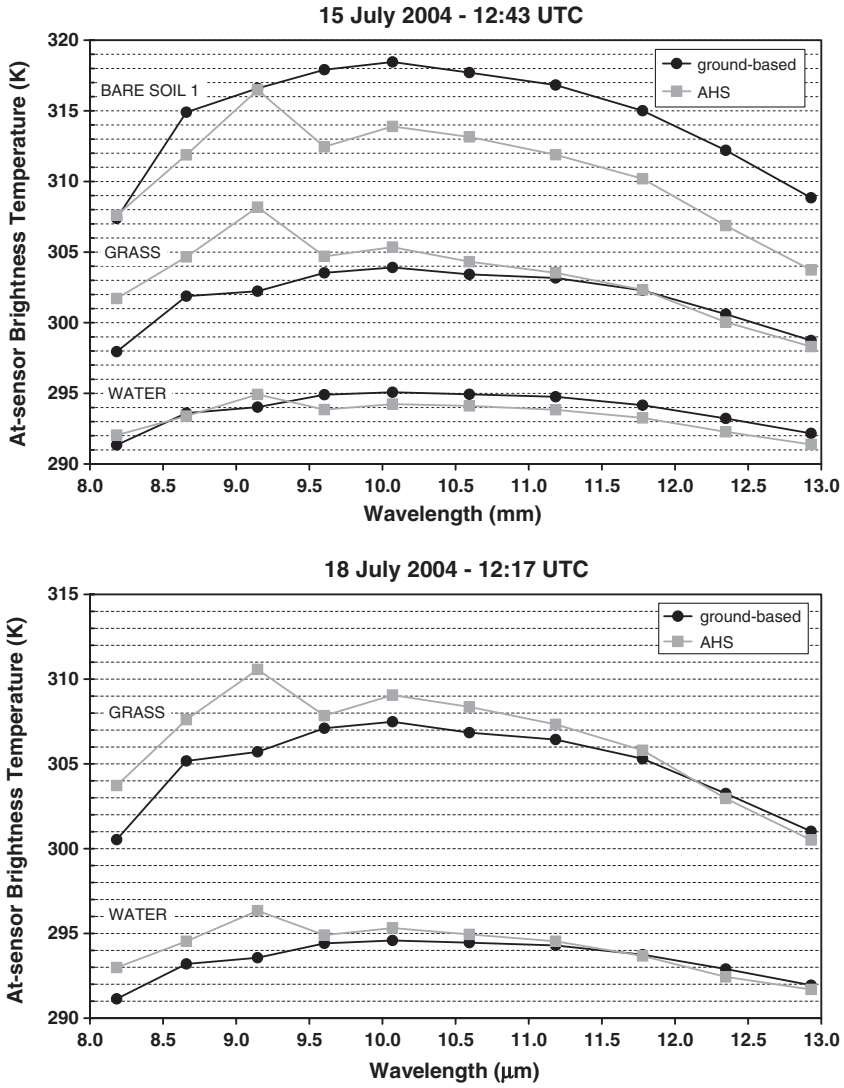

Fig. 7. Comparison between the ground-based and the AHS at-sensor brightness temperature for the high flights (2745 m above ground level) over different surfaces.

the TIGR (TOVS Initial Guess Retrieval) database (Scott & Chedin, 1981) and described in Sobrino et al. (1993b) have been used. In this way, spectral values of the atmospheric parameters τ, $F^{\downarrow}$, and $L^{\uparrow}$ have been obtained. These values have been averaged according to the AHS filter functions in order to obtain the effective values for the thermal bands from 75 to 79 (see Eq. (3)). Fig. 3 showed that the highest τ is obtained for AHS band 75. For this reason, band 75 (10.07 μm) has been chosen as the optimal band for applying the single-channel algorithm given by Eq. (3). The dependence of this algorithm with the atmospheric parameters have been avoided by finding relations with w. Taking into account the set of the 54 radiosoundings mentioned before, the following results have been obtained for the low flight (975 m AGL):

$$\tau_{75} = -0.0505w^2 - 0.0691w + 1.0010$$
$$(R^2 = 0.998,\ \sigma = 0.003) \quad (8)$$

$$L_{75}^{\uparrow} = 0.5638w^2 + 0.4498w - 0.0164$$
$$(R^2 = 0.998,\ \sigma = 0.03\ \mathrm{W \cdot m^{-2} \cdot \mu m^{-1} \cdot sr^{-1}}) \quad (9)$$

$$L_{75}^{\uparrow} = 0.2746w^2 + 3.5473w - 0.2231$$
$$(R^2 = 0.981,\ \sigma = 0.3\ \mathrm{W \cdot m^{-2} \cdot \mu m^{-1} \cdot sr^{-1}}) \quad (10)$$

and for the high flight (2745 m AGL):

$$\tau_{75} = -0.0143w^2 - 0.0678w + 1.0006$$
$$(R^2 = 0.997,\ \sigma = 0.007) \quad (11)$$

$$L_{75}^{\uparrow} = 0.1531w^2 + 0.4900w - 0.0513$$
$$(R^2 = 0.995,\ \sigma = 0.07\ \mathrm{W \cdot m^{-2} \cdot \mu m^{-1} \cdot sr^{-1}}) \quad (12)$$

$$L_{75}^{\downarrow} = 0.0431w^2 + 1.8217w + 0.1503$$
$$(R^2 = 0.976,\ \sigma = 0.3\ \mathrm{W \cdot m^{-2} \cdot \mu m^{-1} \cdot sr^{-1}}) \quad (13)$$

where $L^{\downarrow} \equiv F^{\downarrow}/\pi$, R^2 is the correlation coefficient squared, and σ the standard error of estimation.

In order to select the best combination between the bands i and j involved in the split-window algorithm (see Eq. (16)), the numerical coefficients a_k have been obtained for all the combinations between AHS bands from 75 to 79, and then a

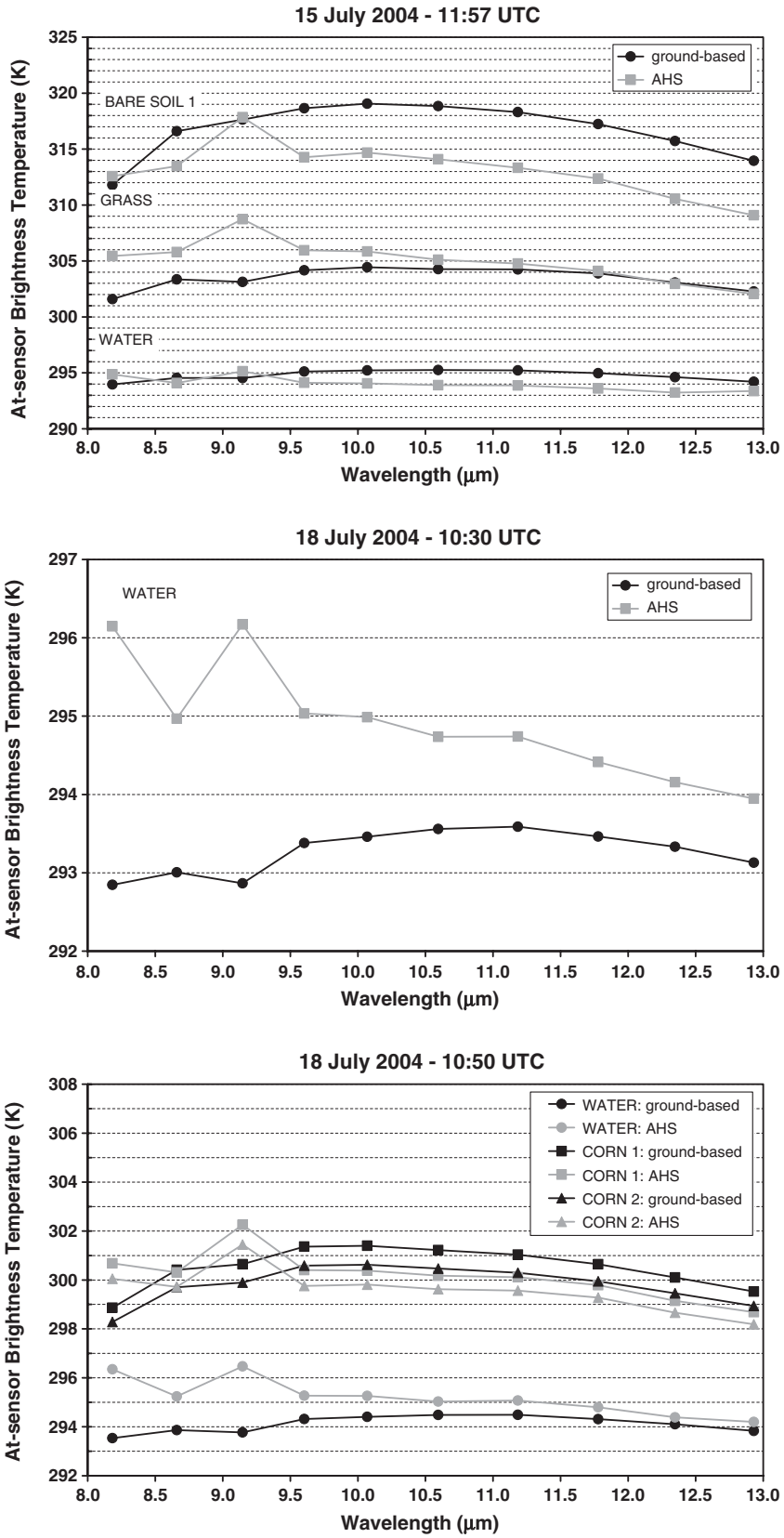

Fig. 8. Comparison between the ground-based and the AHS at-sensor brightness temperature for the low flights (975 m above ground level) over different surfaces.

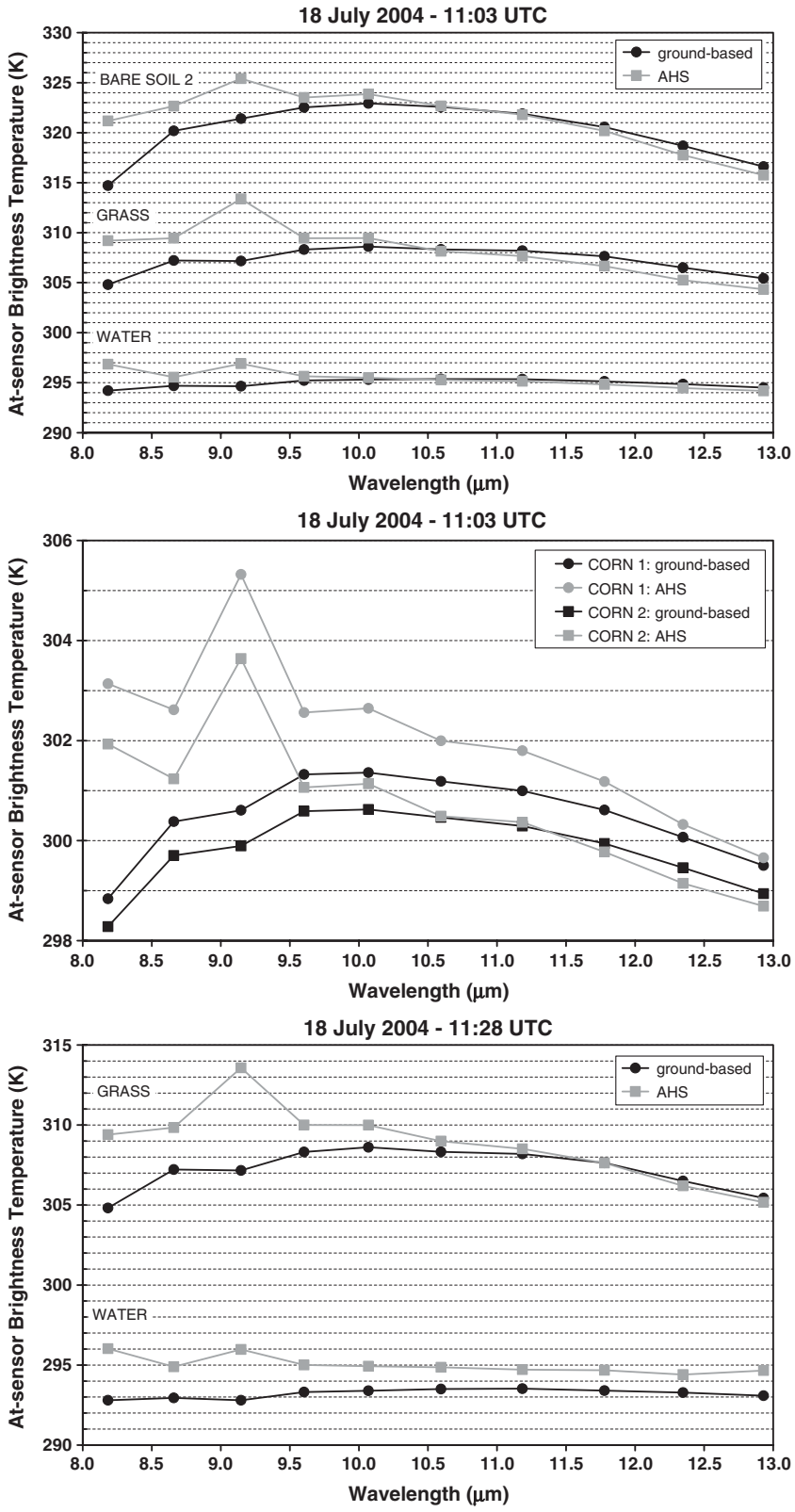

Fig. 8 (*continued*).

sensitivity analysis according to Sobrino et al. (2004) (see Eqs. (10) to (14) in the cited paper) has been carried out in order to estimate the error on the LST retrieved with these algorithms. At-sensor brightness temperatures for the bands i and j involved in Eq. (5) are simulated using the radiative transfer equation (see Eqs. (1) and (2)), in which atmospheric

Table 3
Emissivity spectra extracted from the ASTER spectral library and used in the simulation procedure

Class	Subclass	Samples
Rocks	Igneous	100
	Metamorphics	76
	Sedimentary	68
Soils	Alfisol	9
	Aridisol	14
	Entisol	10
	Inceptisol	7
	Mollisol	9
Vegetation	Green grass	1
	Dry grass	1
	Conifers	1
	Decideous	1
Water–snow–ice	Water	1
	Ice	1
		Total: 299

parameters are obtained again with the MODTRAN 4 code and the set of 54 radiosoundings. In this simulation, surface emissivity values are also needed. A total amount of 299 emissivity spectra extracted from the ASTER spectral library (http://speclib.jpl.nasa.gov) and averaged according to the AHS filter functions have been used in this simulation. All the emissivity spectra correspond to natural surfaces, as is shown in Table 3. Using 54 radiosoundings and 299 emissivity spectra, we obtain 16146 data simulating different atmospheric conditions over different natural surfaces. With this amount of simulated data, statistical fits are applied in order to recover the numerical coefficients involved in the split-window algorithm. The simulated data is also used in the sensitivity analysis (Eqs. (10) to (14) in Sobrino et al., 2004), in order to obtain the theoretical error of the algorithm over different conditions. The mean value of the error and the standard deviation are used in order to compute the root mean square error (RMSE), assumed to be the final theoretical error of the algorithm. The results obtained are shown in Table 4 for the different flight altitudes and also for a typical satellite altitude. Regarding to the low and high flights, the best combination is obtained with AHS bands 75 (10.07 μm) and 79 (12.35 μm). When a satellite altitude is considered, the best combination is obtained with AHS bands 76 (10.59 μm) and 79 (12.35 μm), which agrees with typical split-window combinations used in other thermal sensors as NOAA-AVHRR or ENVISAT-AATSR. In all the cases (low, high, and satellite altitude), the error is around 1 K. The split-window algorithms with the numerical coefficients for the low and high flight are given in Eqs. (14) and (15), respectively:

$$T_s = T_{75} + 0.485(T_{75} - T_{79}) + 0.0068(T_{75} - T_{79})^2 + 0.0798 + (47.15 - 10.80W)(1 - \varepsilon) + (-49.05 + 21.53w)\Delta\varepsilon \quad (14)$$

$$T_s = T_{75} + 0.734(T_{75} - T_{79}) + 0.0096(T_{75} - T_{79})^2 + 0.1198 + (47.46 - 5.20W)(1 - \varepsilon) + (-61.82 + 14.97w)\Delta\varepsilon \quad (15)$$

5.4. Simulated data for the TES method: relation ε_{min}–MMD and testing

The MMD module included in the TES method uses an empirical relationship between the minimum emissivity (ε_{min}) and the spectral contrast (MMD) in order to recover the surface emissivities (Gillespie et al., 1998). This relationship, initially obtained for the ASTER sensor, needs to be recalculated when other sensors are used. The emissivity spectra (299 samples) described in the previous section have been employed to find the relation between ε_{min} and MMD when AHS bands 75 to 79 are considered. Fig. 9 shows the plot of ε_{min} versus MMD for the 299 emissivity spectra of natural surfaces. The following relation has been finally obtained for AHS data:

$$\varepsilon_{min} = 0.986 - 1.350\mathrm{MMD}^{1.019} \quad (16)$$

with a correlation coefficient squared of $R^2 = 0.93$ and a standard error of estimation of $\sigma = 0.019$. It should be noted that the MMD values involved in Eq. (16) have been obtained from AHS bands 75 to 79, located in the 10–12 μm region. In theory, Eq. (16) works better when bands located in the 8–10 μm region are also included. AHS bands located in this region (71 to 74) have not been included due to the calibration problems found (Section 5.2). Despite some problems could arise when using only AHS bands 75 to 79 over high MMD surfaces (rocks), accurate results are expected over low MMD surfaces as agricultural areas. AHS images with no calibration problems will require a new computation for the relationship between ε_{min} and MMD.

The TES method has been tested using the simulated data described in the previous section for different flight altitudes: 700 km, 975 m, and 2745 m. The LST retrieved with the method has been compared with the LST included in the simulated data and extracted from the radiosoundings. In all the cases, the TES method provided a RMSE < 1.1 K.

Table 4
Error on the land surface temperature retrieved with the split-window algorithm given in Eq. (5) for different combinations between AHS thermal bands and for different flight altitudes

Band 'i'	Band 'j'	Low flight (975 m AGL)	High flight (2745 m AGL)	Satellite altitude (700 km AGL)
		Error (K)	Error (K)	Error (K)
75	76	1.3	1.8	1.6
75	77	1.2	1.3	1.6
75	78	1.2	1.1	1.7
75	79	**1.1**	**1.0**	1.6
76	77	2.2	2.6	3.0
76	78	1.7	1.6	1.8
76	79	1.4	1.1	**1.2**
77	78	2.4	2.6	3.0
77	79	1.7	1.5	1.6
78	79	2.4	2.3	2.3

The minimum error in each case is highlighted.

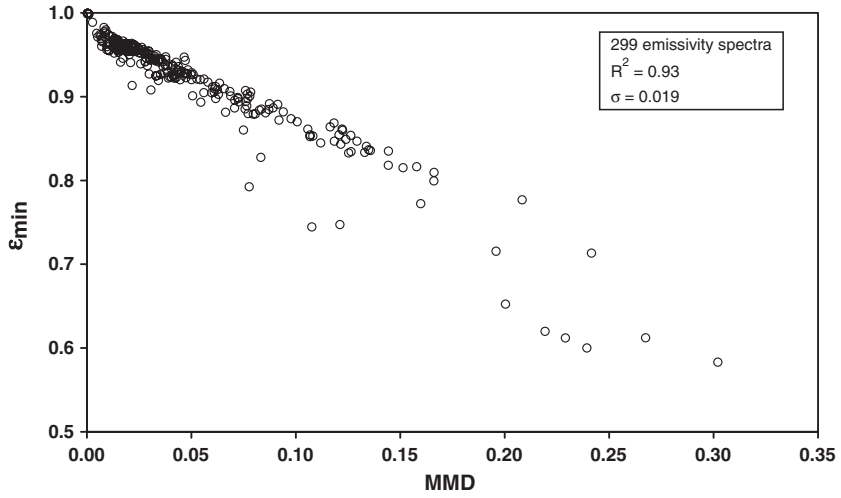

Fig. 9. Empirical relationship between minimum emissivity (ε_{min}) and spectral contrast (MMD) obtained from the emissivity spectra described in Table 3 (R^2 is the correlation coefficient squared and σ is the standard error of estimation).

5.5. Algorithms validation with ground truth data

The algorithms described in the previous sections have been validated using the field measurements carried out in the framework of the different field campaigns. Single-channel and two-channel methods have been tested in the framework of the SPARC/EAGLE and AGRISPECTRA field campaigns. In the SPARC/EAGLE campaign, a total amount of 17 plots composed by water, grass, bare soil, and corn have been used, whereas in the AGRISPECTRA campaign a total amount of 30 plots have been used (10 trees per flight). In order to apply the TES method, an accurate estimation of the atmospheric parameters is needed, since it uses atmospherically corrected data. In the SPARC/EAGLE campaign, different radiosoundings were launched almost simultaneously with the sensor overpass. However, in the AGRISPECTRA campaign, radiosounding data or atmospheric characterizations were not available, so TES method has been only tested in the framework of the SPARC/EAGLE campaign. The values of atmospheric water vapour content needed in order to apply the single-channel and split-window algorithms are given in Table 5. These values have been obtained using the radiosoundings launched in situ in the framework of the SPARC/EAGLE campaigns and the MODTRAN 4 radiative transfer code. In the AGRISPECTRA campaign, no radisoundings were launched, as has been commented before, so in this case we only have the value measured with a sunphotometer in the "El Arenosillo" site, located around 250 km far from the field and which is included in the AERONET (Aerosol Robotic Network). Details can be found at http://aeronet.gsfc.nasa.gov. The total water vapour content extracted from the AERONET data has been scaled to the altitude of the flight (980 m AGL) using the MODTRAN 4 code and assuming the atmospheric profile included in the midlatitude summer atmosphere.

The test of the single-channel method is shown in Fig. 10a for the SPARC/EAGLE and in Fig. 10b for AGRISPECTRA, with RMSE values of 1.6 K and 1.9 K, respectively. The Bias has been calculated as the mean value for the difference between the LST retrieved with the algorithm and the measured in situ. In both cases, the Bias is positive, which indicates that the algorithm overestimates the LST. This overestimation is more clearly shown in the results achieved in the AGRISPECTRA campaign, with a Bias of 1.7 K. We attribute this to the poor characterization of the atmosphere during this experiment, in which a water vapour value measured 250 km far from the field site has been chosen. The results obtained with the single-channel algorithm proposed in this paper agree with those obtained by Jiménez-Muñoz and Sobrino (2005) also from high resolution data over the Barrax test site, with RMSE < 1.8 K.

Results obtained with the split-window algorithm are shown in Fig. 11, in which RMSE values of 1.9 K and 1.6 K have been obtained for the SPARC/EAGLE and AGRISPECTRA campaigns, respectively. In this last case, the Bias is lower than the obtained with the single-channel method, which indicates that the split-window is less sensitive to an accurate knowledge of the water vapour content. Additional results obtained with the split-window algorithm in the AGRISPECTRA campaign can be found in Sepulcre-Cantó et al. (in press). Despite similar

Table 5
Atmospheric water vapour content (w) at different altitudes

Campaign	Date	Altitude (km AGL)	w (g/cm^2)
SPARC/EAGLE	15-July-2004	0.975	0.71
SPARC/EAGLE	15-July-2004	0.975	1.49
SPARC/EAGLE	15-July-2004	100	1.66
SPARC/EAGLE	18-July-2004	2.745	0.79
SPARC/EAGLE	18-July-2004	2.745	1.58
SPARC/EAGLE	18-July-2004	100	1.74
AGRISPECTRA	25-July-2004	0.980	0.90
AGRISPECTRA	25-July-2004	100	2.54

Values for the SPARC/EAGLE campaign have been obtained using the radiosoundings launched in situ and the MODTRAN 4 code. Water vapour for the AGRISPECTRA campaign has been obtained from the AERONET network and measured with a sunphotometer in the "El Arenosillo" site, around 250 km far from the field. Total content has been rescaled using the MODTRAN 4 and assuming a midlatitude summer atmosphere in order to obtain the value for an altitude of 980 m.

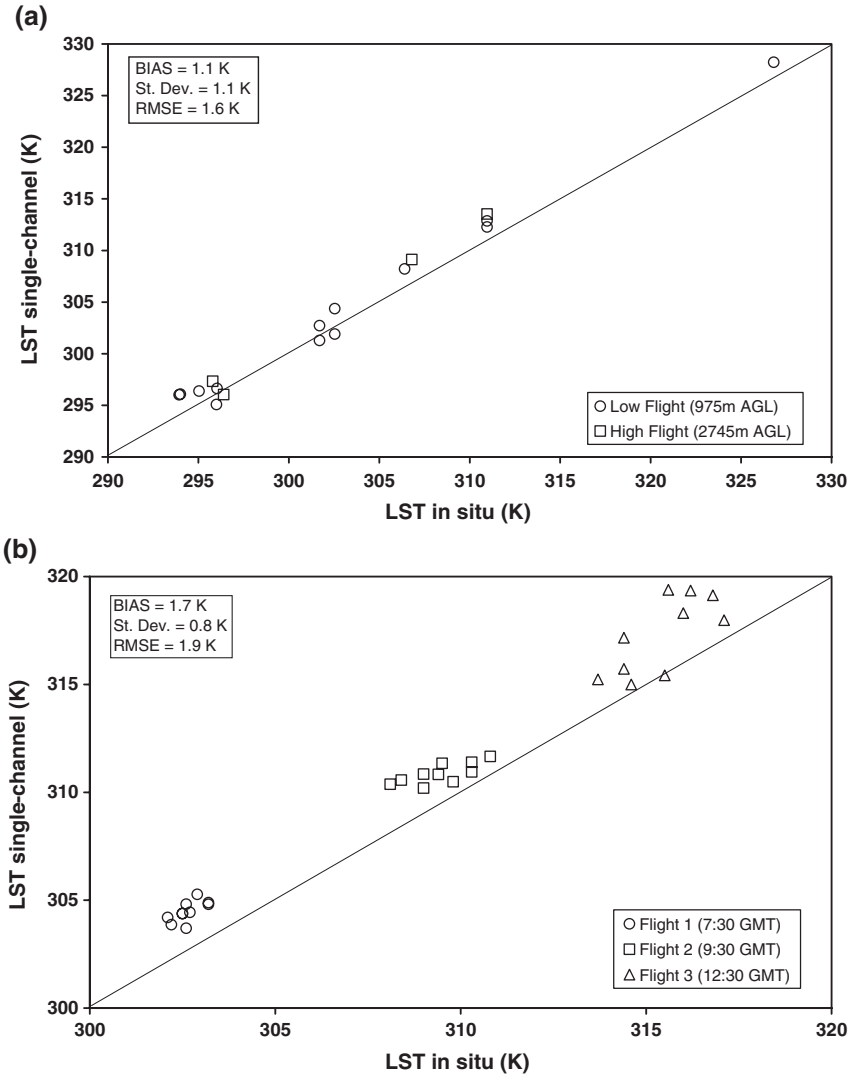

Fig. 10. Comparison between the land surface temperature retrieved with the single-channel method and the one measured in situ in the framework of the (a) SPARC/EAGLE and (b) AGRISPECTRA field campaigns.

results have been obtained with split-window and single-channel algorithms, the split-window technique provides better results over a world-wide scale, overall in wet atmospheres ($w>3\,g/cm^2$), whereas single-channel methods only provide good results for low atmospheric absorption ($w<2\,g/cm^2$), as has been stated by Sobrino and Jiménez-Muñoz (2005).

Fig. 12 shows the results obtained with the TES method in the framework of the SPARC/EAGLE campaign. This method provides the best estimation of the LST, with a RMSE of 1.4 K. The Bias is similar to the previous algorithms, around 1 K. This result suggests that from sensors providing multispectral thermal data (with at least four thermal bands) it is possible to retrieve the LST with slightly better accuracy. However, the main constraint is that the atmospheric correction needs to be well controlled.

Finally, Fig. 13 shows the AHS image (acquired on 15 July 2004 at 12:43 UTC) for the at-sensor brightness temperature obtained from band 75, the LST image obtained with the TES method and the difference image. This difference shows the impact of the emissivity and atmospheric effects on the LST retrieval. Differences between temperatures obtained from at-sensor data and the ones obtained after compensation of atmospheric and emissivity effects range between 2 and 5 K. The lowest differences (<2 K) are obtained over vegetated areas and water (dark tones in the image), in which the emissivity is near to 1 and the differences are only due to the atmospheric effect. This example shows the importance of the atmospheric and emissivity correction in order to obtain accurate values of LST.

6. Summary and conclusions

Land surface temperature (LST) is a key parameter in many environmental studies, as energy balance, evapotranspiration, global circulation models, and vegetation monitoring, among others. In the last years, different airborne sensors with several thermal bands have been developed and made available for imagery acquisitions. The data extracted from these sensors provide the opportunity of retrieving LST with a very-high spatial resolution, which is important, for example, in the

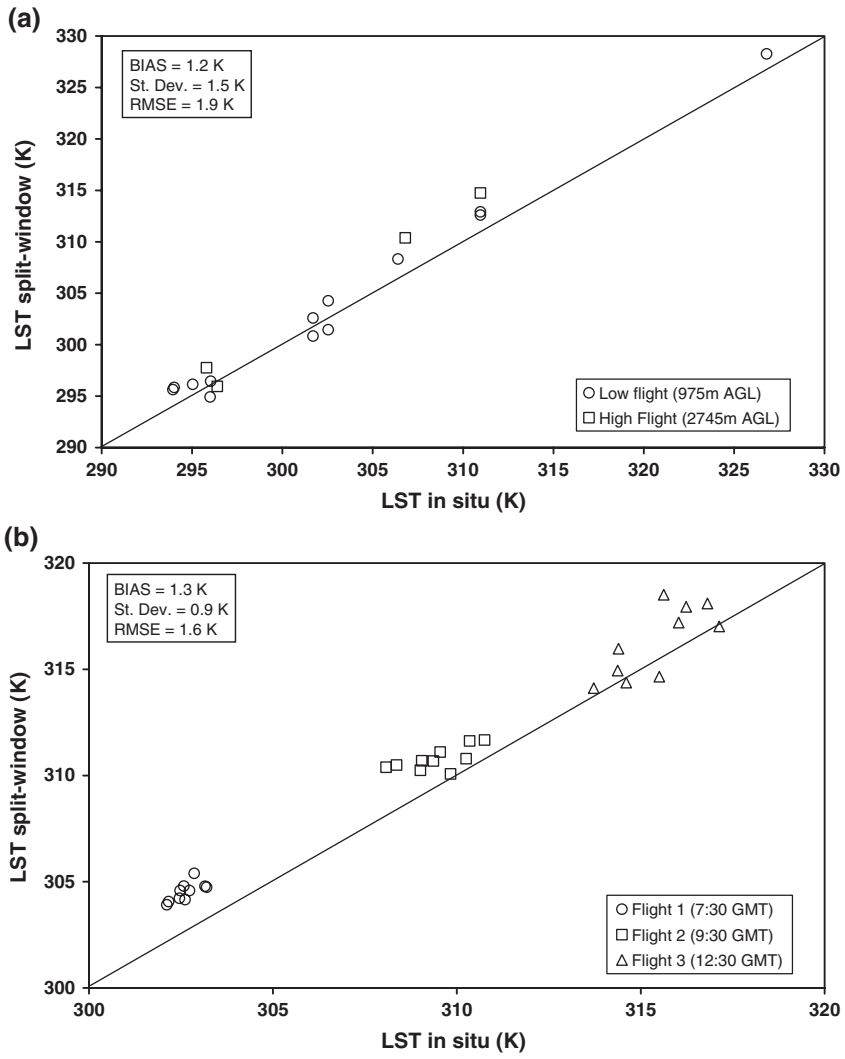

Fig. 11. Comparison between the land surface temperature retrieved with the split-window method and the one measured in situ in the framework of the (a) SPARC/EAGLE and (b) AGRISPECTRA field campaigns.

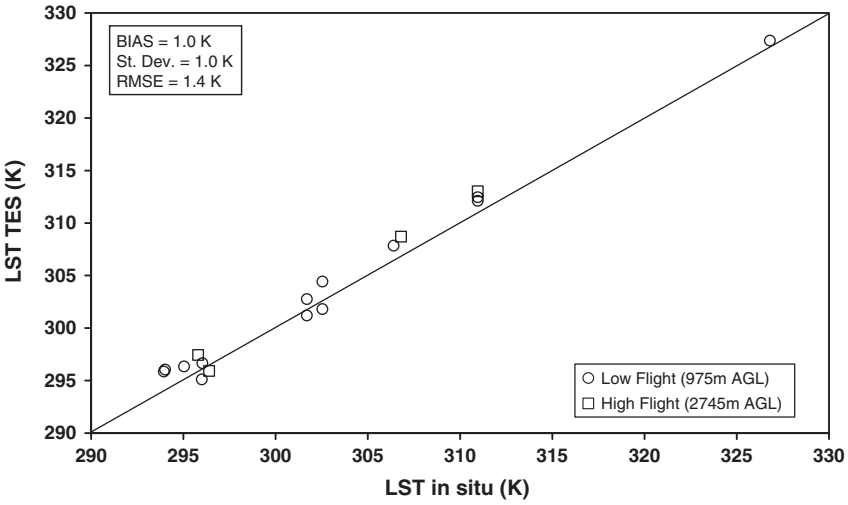

Fig. 12. Comparison between the land surface temperature retrieved with the TES method and the one measured in situ in the framework of the SPARC/EAGLE field campaign.

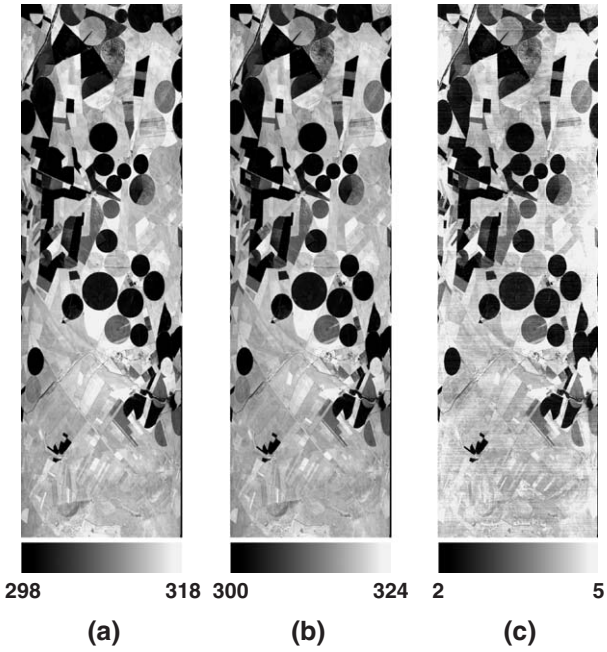

Fig. 13. (a) At-sensor brightness temperature obtained from the AHS band 75 (T75), (b) land surface temperature (LST) obtained with the TES method and (c) difference image (ΔT=LST − T75). The AHS image was acquired on 15 July 2005 over the Barrax test site (see Fig. 1) at 12:43 UTC and the spatial resolution is 7 m. Temperature values are given in K.

context of precision agriculture and vegetation stress monitoring. The airborne hyperspectral scanner (AHS) sensor, with 10 thermal bands (from 71 to 80) covering the range between 8 and 13 μm, is an example of the new generation of airborne sensors with multispectral thermal infrared capabilities.

The feasibility of retrieving LST from the 10 AHS thermal bands has been analyzed in the framework of the SPARC and EAGLE field campaigns, which took place simultaneously in the Barrax (Albacete, Spain) test site, and in the framework of the AGRISPECTRA project, which took place in an orchard crop field in Córdoba (Spain), all of them in July 2004. For this purpose, the single-channel, split-window, and TES (temperature and emissivity separation) methods have been adapted to the AHS characteristics. Previously, the at-sensor brightness temperatures extracted from the AHS thermal bands were compared with in situ measurements carried out over different plots (bare soil, water, grass, and corn) in order to assess the optimal selection of bands for LST retrieval. This comparison has shown that the AHS sensor had a calibration problem with bands 71, 72, and 73. Bands from 75 to 79, located in the atmospheric window between 10 and 12 μm, seem to agree better with in situ data, so these bands were finally selected. The single-channel method, which only uses one thermal band, was applied to AHS band 75 because this band showed the highest atmospheric transmissivity. The split-window algorithm, which used a combination between two thermal bands, was applied to AHS bands 75 and 79, because this combination showed the lowest error on the LST. Both algorithms were validated using ground truth data, showing similar results, with root mean square errors (RMSE) lower than 2 K. The good results obtained with the single-channel method are attributed to the low atmospheric absorption during the flights, with total atmospheric water vapour contents lower than 1.8 g/cm^2 for the high flights (2745 m above ground level) and lower than 1 g/cm^2 for the low flights (945 m above ground level). With higher water vapour contents and, therefore, with higher atmospheric absorption, the split-window algorithms are expected to provide better results, whereas single-channel algorithms become almost unusable (Sobrino & Jiménez-Muñoz, 2005). The TES method, developed originally for the ASTER sensor by Gillespie et al. (1998), was applied to AHS bands from 75 to 79, and it was also tested with simulated data, with a RMSE < 1.1 K. The TES method provided the best result in the validation with ground truth data, with a RMSE < 1.4 K. It should be noted that this method also provides land surface emissivities, which are assumed to be known a priori in the single-channel and split-window methods, despite that the emissivity spectra obtained with the TES have not been tested or validated. According to the results obtained in this study, the use of multispectral thermal data leads to a more accurate values of surface temperatures, albeit slightly, and it also solves the problem of the emissivity uncertainty. However, an accurate atmospheric correction should be performed to the sensor data in order to obtain the good results pointed out.

Acknowledgements

We thank the European Union (EAGLE, project SST3-CT-2003-502057), the Ministerio de Ciencia y Tecnología (DATASAT, project ESP2005-07724-C05-04), and the European Space Agency (SPARC, project 18307/04/NL/FF) for the financial support. Funding support provided for the Agrispectra project AGL2002-04407-C03 from the Spanish MCyT is acknowledged. We also thank Don Sabol (University of Washington) and Cindy Grove (Jet Propulsion Laboratory) for laboratory measurements of soil spectra.

References

Balick, L. K., Jeffery, C. A., & Henderson, B. G. (2003). Turbulence-induced spatial variation of surface temperature in high-resolution thermal IR satellite imagery. *Proceedings of SPIE*, *vol. 4879* (pp. 221–230). Crete, Greece, SPIE—the International Society for Optical Engineering.

Becker, F., & Li, Z. -L. (1990a). Temperature independent spectral indices in thermal infrared bands. *Remote Sensing of Environment*, *32*, 17−33.

Becker, F., & Li, Z. -L. (1990b). Towards a local split window method over land surfaces. *International Journal of Remote Sensing*, *11*, 369−394.

Berk, A., Anderson, G. P., Acharya, P. K., Chetwynd, J. H., Bernstein, L. S., Shettle, E. P., et al. (1999). *MODTRAN4 user's manual*. Hanscom AFB, MA: Air Force Research Laboratory.

Dash, P., Göttsche, F. -M., Olesen, F. -S., & Fischer, H. (2002). Land surface temperature and emissivity estimation from passive sensor data: Theory and practice—current trends. *International Journal of Remote Sensing*, *23*(13), 2563−2594.

Deschamps, P. Y., & Phulpin, T. (1980). Atmospheric correction of infrared measurements of sea surface temperature using channels at 3.7, 11 and 12 μm. *Boundary-Layer Meteorology*, *18*, 131−143.

Gillespie, A., Rokugawa, S., Matsunaga, T., Cothern, J. S., Hook, S., & Kahle, A. B. (1998). A temperature and emissivity separation algorithm for advanced spaceborne thermal emission and reflection radiometer (ASTER) images. *IEEE Transactions on Geoscience and Remote Sensing*, *36*, 1113−1126.

Jiménez-Muñoz, J. C., & Sobrino, J. A. (2003). A generalized single-channel method for retrieving land surface temperature from remote sensing data. *Journal of Geophysical Research*, *108*(D22). doi:10.1029/2003JD003480.

Jiménez-Muñoz, J. C., & Sobrino, J. A. (2005). Atmospheric water vapour content retrieval from visible and thermal data in the framework of the DAISEX campaigns. *International Journal of Remote Sensing*, *26*(15), 3163−3180.

Kerr, Y. H., Lagouarde, J. P., Nerry, F., & Ottlé, C. (2004). Land surface temperature retrieval techniques and applications: Case of AVHRR. In D. A. Quattrochi, & J. C. Luvall (Eds.), *Thermal remote sensing in land surface processes* (pp. 33−109). Florida, USA: CRC Press.

Kondratyev, K. Y. (1969). *Radiation in the atmosphere.* New York: Academic Press.

McClain, E. P., Pichel, W. G., & Walton, C. C. (1985). Comparative performance of AVHRR-based multichannel sea surface temperatures. *Journal of Geophysical Research*, *90*(11), 587−601.

McMillin, L. M. (1975). Estimation of sea surface temperature from two infrared window measurements with different absorption. *Journal of Geophysical Research*, *80*, 5113−5117.

Moreno, J., Calera, A., Caselles, V., Cisneros, J. M., Martínez-Lozano, J. A., Meliá, J., et al. (2001). The measurement programme at Barrax. *DAISEX final results workshop, SP-499* (pp. 43−51). Noordwijk (Holland): ESA Publications Division.

Nerry, F., Labed, J., & Stoll, M. P. (1990). Spectral properties of lands surfaces in the thermal infrared band: Part II. Field method for spectrally averaged emissivity measurements. *Journal of Geophysical Research*, *95*, 7027−7044.

Prata, A. J. (1993). Land surface temperatures derived from the AVHRR and ATSR: 1. Theory. *Journal of Geophysical Research*, *89*(16), 689−702.

Price, J. C. (1984). Land surface temperature measurements from the split window channels of the NOAA 7 AVHRR. *Journal of Geophysical Research*, *89*, 7231−7237.

Qin, Z., Karnieli, A., & Berliner, P. (2001). A mono-window algorithm for retrieving land surface temperature from Landsat TM data and its application to the Israel–Egypt border region. *International Journal of Remote Sensing*, *22*(18), 3719−3746.

Quattrochi, D. A., & Luvall, J. C. (1999). Thermal infrared remote sensing data for analysis of landscape ecological processes: Methods and applications. *Landscape Ecology*, *14*(6), 577−598.

Quattrochi, D. A., & Luvall, J. C. (2004). *Thermal remote sensing in land surface processes* (pp. 440). Boca Raton, FL, USA: CRC Press.

Scott, N. A., & Chedin, A. (1981). A fast line by line method for atmospheric absorption computations: The authomatized atmospheric absorption atlas. *Journal of Meteorology*, *20*, 802−812.

Sepulcre-Cantó, G., Zarco-Tejada, P.J., Jiménez-Muñoz, J.C., Sobrino, J.A., de Miguel, E., Villalobos, F.J., in press. Within-field thermal variability detection as function of water stress in *Olea europaea* L. orchards with high-spatial remote sensing imagery. *Agricultural and Forest Meteorology* (available online).

Sobrino, J. A., Caselles, V., & Coll, C. (1993). Theoretical split window algorithms for determining the actual surface temperature. *Il Nuovo Cimento*, *16*, 219−236.

Sobrino, J. A., Coll, C., & Caselles, V. (1991). Atmospheric correction for land surface temperature using NOAA-11 AVHRR Channels 4 and 5. *Remote Sensing of Environment*, *38*, 19−34.

Sobrino, J. A., & Jiménez-Muñoz, J. C. (2005). Land surface temperature retrieval from thermal infrared data: An assessment in the context of the Surface Processes and Ecosystem Changes Through Response Analysis (SPECTRA) mission. *Journal of Geophysical Research*, *110*(D16103). doi:10.1029/2004JD005588.

Sobrino, J. A., Jiménez-Muñoz, J. C., El-Kharraz, J., Gómez, M., Romaguera, M., & Sòria, G. (2004). Single-channel and two-channel methods for land surface temperature retrieval from DAIS data and its application to the Barrax test site. *International Journal of Remote Sensing*, *25*(1), 215−230.

Sobrino, J. A., Li, Z. -L., Soria, G., & Jiménez, J. C. (2002). Land surface temperature and emissivity retrieval from remote sensing data. *Recent Research Developments on Geophysics*, *4*, 21−44.

Sobrino, J. A., Li, Z. -L., & Stoll, M. P. (1993). Impact of the atmospheric transmittance and total water vapor content in the algorithms for estimating satellite sea surface temperatures. *IEEE Transactions on Geoscience and Remote Sensing*, *31*(5), 946−952.

Sobrino, J. A., Li, Z. -L., Stoll, M. P., & Becker, F. (1994). Improvements in the split-window technique for land surface temperature determination. *IEEE Transactions on Geoscience and Remote Sensing*, *32*, 243−253.

Sobrino, J. A., & Raissouni, N. (2000). Toward remote sensing methods for land cover dynamic monitoring. Application to Morocco. *International Journal of Remote Sensing*, *21*, 353−366.

Sun, D., & Pinker, R. T. (2003). Estimation of land surface temperature from a Geostationary Operational Environmental Satellite (GOES-8). *Journal of Geophysical Research*, *108*(D11). doi:10.1029/2002JD002422.

Wan, Z., & Li, Z. -L. (1997). A physics-based algorithm for retrieving land surface emissivity and temperature from EOS/MODIS data. *IEEE Transactions on Geoscience and Remote Sensing*, *35*(4), 980−996.